Dalton Transactions

ROYAL SOCIETY OF CHEMISTRY

PAPER

View Article Online
View Journal | View Issue

Cite this: *Dalton Trans.*, 2025, **54**, 9984

Modelling the binding of cytotoxic dinuclear nickel complexes to two neighboring phosphate esters of DNA using dicarboxylate ligands†

Thomas Riediger, Maximilian Böhm, Michael Kapiza, Anja Stammler, Jan Oldengott and Thorsten Glaser *

The cytotoxic complex [(Htom$^{6\text{-Me}}$){Ni^{II}(OAc)}$_2$](OAc) (H_2tom$^{6\text{-Me}}$ = 2,7-bis(di(6-methylpyridine-2-yl-methyl)aminomethyl)-1,8-naphthalenediol) is supposed to bind in the aquated form [(Htom$^{6\text{-Me}}$){Ni^{II}(OH$_2$)$_2$}$_2$]$^{3+}$ to two neighboring phosphate diesters of the DNA backbone. To further support this intended molecular mode of action, difunctional ligands in the form of the dicarboxylates succinate and glutarate are used here to mimic two neighboring phosphates of the DNA backbone. The complex [(Htom$^{6\text{-Me}}$){Ni^{II}(OAc)}$_2$](OAc) is treated with 3 equiv. HCl to protonate the acetates providing presumably [(Htom$^{6\text{-Me}}$){Ni^{II}(OH$_2$)$_2$}$_2$]$^{3+}$, which is reacted with the dicarboxylates yielding the complexes [(Htom$^{6\text{-Me}}$){Ni^{II}(μ-succ)Ni^{II}}]$^{+}$ and [(Htom$^{6\text{-Me}}$){Ni^{II}(μ-glut)Ni^{II}}]$^{+}$ confirmed by single-crystal X-ray diffraction. The sterical constraints of the dicarboxylates enforces shorter Ni···Ni distances demonstrating the flexibility of the coordination compartments despite the rigid 1,8-naphthalenediol backbone. These steric constraints by the pull effect of the organic spacers affect the Ni^{II}–ligand bonds and are reflected in FTIR and UV-Vis-NIR spectroscopic but not magnetic signatures. The comparison to a related Cu^{II} complex indicates a severe impact of the 6-methyl groups of the pyridine donors on the relative orientation of the anticipated phosphate binding sites in these complexes. The consequences for a rational strengthening of the binding to DNA and hence increase of the cytotoxicity by possible ligand modifications are discussed.

Received 21st April 2025,
Accepted 1st June 2025

DOI: 10.1039/d5dt00941c

rsc.li/dalton

Introduction

Cisplatin[1] and related complexes are a potent class of anticancer drugs.[2] It is supposed that a platinum-based complex fragment binds to the nucleobases of DNA that interferes with cellular processes leading finally to apoptosis. Although many new platinum-based complexes were synthesized and tested, several types of cancer cannot be treated with cisplatin-based drugs and there is a development of resistance of cancer cells towards cisplatin-based drugs.[3] The serious toxicity of platinum-based anticancer drugs stimulated research for more biorelevant metal ions especially of the first row.[4]

In order to allow a new and different molecular mode of action, we intended to coordinate not to the nucleobases but to the phosphate diesters of the DNA backbone. To increase the binding affinity to the oxygen atoms of the phosphate diesters, our ligand design was based on the multivalence-principle.[5] The binding should occur to two neighboring phosphate diesters of the DNA backbone by molecular recognition with two phosphate binding sites held by a rigid backbone at the distance of two neighboring phosphate esters in the DNA backbone of 6–7 Å. Sterical demand around the phosphate binding sites should prevent the binding to the less exposed nucleobases. These design guidelines led to the new family of 2,7-disubstituted 1,8-naphthalenediol ligands with bulky pendant arms in the 2,7-position (Scheme 1).[6] Indeed, the complexes [(Htom$^{6\text{-Me}}$){Cu^{II}(OAc)}$_2$](OAc) and [(Htom$^{6\text{-Me}}$){Ni^{II}(OAc)}$_2$](OAc) bind to DNA, interfere with DNA synthesis in PCR at lower concentrations than cisplatin, and kill human cancer cells more efficiently than human stem cells of the same proliferation rate.[7] We have shown a preferential binding of phosphate diester models that exchanges the coordinated acetates.[8,9] Infrared multiple photon dissociation (IRMPD) spectroscopy[10] showed the binding to the phosphates in nucleobases and high resolution ultra-high vacuum atomic force microscopy (HR-UHV-AFM) provided strong evidence for the binding of the complexes to the phosphate diesters of the DNA backbone.[11]

Despite this evidence, a direct proof of the intended binding mode of the dinuclear complexes to two neighboring phosphate diesters of the DNA backbone is still missing. To

Lehrstuhl für Anorganische Chemie I, Fakultät für Chemie, Universität Bielefeld, Universitätsstr. 25, D-33615 Bielefeld, Germany.
E-mail: thorsten.glaser@uni-bielefeld.de

†Electronic supplementary information (ESI) available. CCDC 2445426 and 2445427. For ESI and crystallographic data in CIF or other electronic format see DOI: https://doi.org/10.1039/d5dt00941c

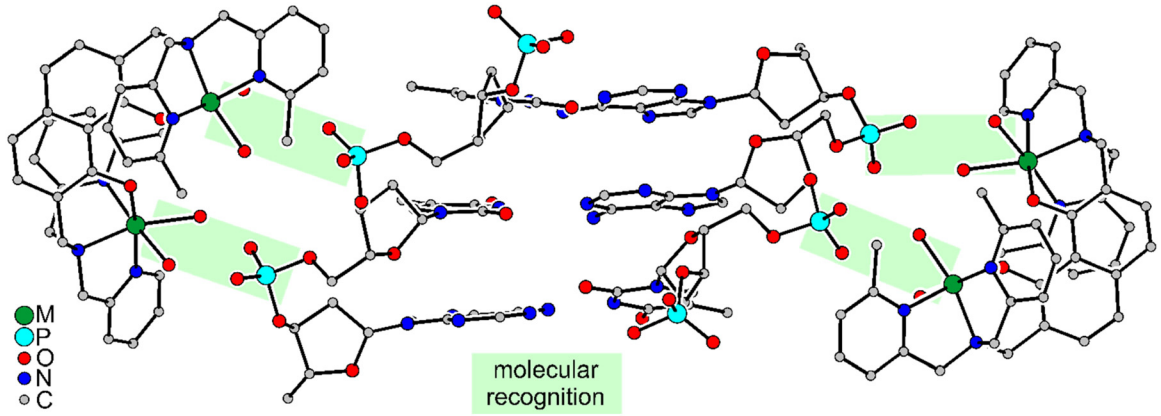

Scheme 1 Intended molecular recognition of two neighboring phosphate diesters of the DNA backbone by dinuclear complexes with a 2,7-di-substituted 1,8-naphthalenediol ligand.

further support this binding mode, we thought to use difunctional ligands, *i.e.* ligands that exhibit two binding sites to better model two neighboring phosphate diesters of the DNA backbone. In a first attempt, we used glutaric acid (pentanedioic acid, H_2glut). However, the reaction of $[(Htom^{6\text{-}Me})\{Cu^{II}(OAc)\}_2](OAc)$ with glutaric acid did not provide the intended dinuclear complex $[(Htom^{6\text{-}Me})\{Cu^{II}(\mu\text{-glut})Cu^{II}\}]^+$ with an intramolecular glutarate bridge but the tetranuclear macrocycle $[\{(Htom^{6\text{-}Me})Cu^{II}_2\}_2(\mu\text{-glut})_2]^{2+}$, where the two carboxylate donors of one glutarate do not bind to the Cu^{II} ions of the same dinuclear complex fragment $[(Htom^{6\text{-}Me})Cu^{II}_2]^{3+}$ but to two of these fragments.[12] Here, we present the successful reaction of the difunctional ligands glutaric acid and succinic acid (butanedioic acid, H_2succ) with $[(Htom^{6\text{-}Me})\{Ni^{II}(OAc)\}_2](OAc)$ providing the dinuclear complexes $[(Htom^{6\text{-}Me})\{Ni^{II}(\mu\text{-glut})Ni^{II}\}]^+$ and $[(Htom^{6\text{-}Me})\{Ni^{II}(\mu\text{-succ})Ni^{II}\}]^+$, respectively, (Scheme 2) where the two intramolecularly bridging dicarboxylates mimic the molecular recognition of the complex fragment $[(Htom^{6\text{-}Me})Ni^{II}_2]^{3+}$ with two neighboring phosphate sites of DNA.

Experimental section

Solvents and starting materials were of the highest commercially available purity and used as received. The complex $[(Htom^{6\text{-}Me})\{Ni^{II}(OAc)\}_2](OAc)$ was synthesized according to the procedure reported previously.[7]

$[(Htom^{6\text{-}Me})\{Ni^{II}(\mu\text{-succ})Ni^{II}\}](BPh_4)\cdot 2CH_3CN$

A solution of hydrochloric acid (557 μmol, 3.0 equiv.) in MeOH (6 mL) and H_2O (2 mL) was added to a dark green solution of $[(Htom^{6\text{-}Me})\{Ni^{II}(OAc)\}_2](OAc)\cdot 9H_2O$ (206 mg, 188 μmol, 1 equiv.) in MeOH (10 mL) at 40 °C, which resulted in a light green solution. After stirring for 30 minutes at 40 °C, the solution was added to a solution of $NaBPh_4$ (391 mg, 1.14 mmol, 6.1 equiv.) in MeOH (4.5 mL) and H_2O (0.5 mL) at room temperature. The resulting precipitate was isolated and complete precipitation was enforced by adding H_2O to the filtrate. The combined solids were washed with H_2O and redissolved in CH_3CN (13.3 mL) and H_2O (0.7 mL). A solution of NEt_3 (54.0 μL, 390 μmol, 2.1 equiv.) and succinic acid (23 mg,

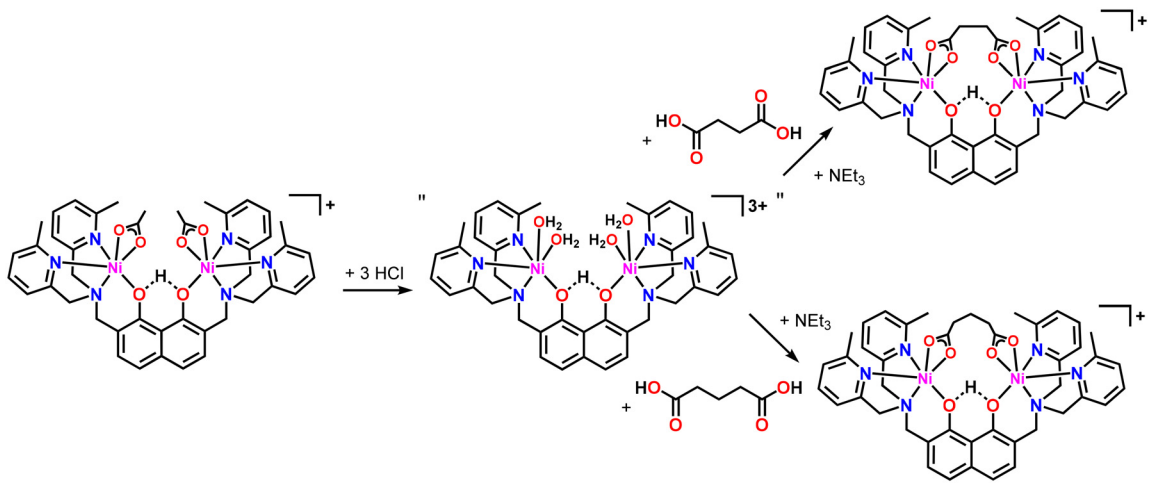

Scheme 2 Synthesis of complexes.

195 μmol, 1.0 equiv.) in CH_3CN (13.3 mL) and H_2O (0.7 mL) was added. The solution was stirred at ambient temperatures for 15 minutes and filtered. Diffusion of Et_2O into the filtrate provided dark green crystals, which were suitable for single-crystal X-ray diffraction. The crystals were filtered off and washed three times with Et_2O. Yield: 228 mg (179 μmol, 95%). ESI-MS (pos. mode, CH_3CN): m/z = 869.1 $[(Htom^{6\text{-}Me})\{Ni^{II}(\mu\text{-succ})Ni^{II}\}]^+$. IR (KBr): $\tilde{\nu}/cm^{-1}$ = 3055 m, 3033 m, 2999 w, 2984 w, 2923 w, 2846 w, 2247 w, 1951 w, 1885 w, 1827 w, 1770 w, 1608 s, 1579 s, 1541 s, 1468 s, 1450 s, 1400 m, 1370 m, 1335 m, 1308 w, 1299 w, 1273 w, 1244 w, 1166 m, 1138 w, 1121 w, 1099 w, 1085 w, 1056 m, 1032 w, 1016 w, 1000 w, 970 w, 892 m, 828 m, 791 m, 750 m, 734 s, 707 s, 612 m, 512 w, 452 w. UV-Vis-NIR (2,2,2-trifluoroethanol): $\tilde{\nu}/cm^{-1}$ (ε/M^{-1} cm^{-1}) = 42 800 (47 400), 37 700 (18 700), 36 600 (14 400), 30 900 (5100), 29 300 (8000), 28 200 (10 500), 22 300 (42), 21 200 (37), 20 900 (38), 20 000 (27), 19 500 (28), 16 800 (24), 12 600 (11), 10 300 (27). Anal. calcd for $[(Htom^{6\text{-}Me})\{Ni^{II}(\mu\text{-succ})Ni^{II}\}](BPh_4)\cdot 2CH_3CN$ ($C_{72}H_{71}BN_8Ni_2O_6$): C 67.95, H 5.62, N 8.81%. Found: C 68.06, H 5.81, N 8.60%.

$[(Htom^{6\text{-}Me})\{Ni^{II}(\mu\text{-glut})Ni^{II}\}](BPh_4)\cdot 2CH_3CN$

A solution of hydrochloric acid (296 μmol, 3.0 equiv.) in H_2O (6 mL) was added to a dark green solution of $[(Htom^{6\text{-}Me})\{Ni^{II}(OAc)\}_2](OAc)\cdot 5H_2O\cdot 0.1ACN$ (102 mg, 99.4 μmol, 1 equiv.) in H_2O (10 mL) at 40 °C. The resulting light green solution was stirred for 10 minutes at 40 °C, cooled to ambient temperature, and added to a solution of $NaBPh_4$ (204 mg, 596 mmol, 6.0 equiv.) in H_2O (5 mL). The precipitate was filtered off, washed with H_2O, redissolved in CH_3CN (15 mL), and treated with a solution of NEt_3 (29.0 μL, 209 μmol, 2.1 equiv.) and glutaric acid (13.8 mg, 105 μmol, 1.1 equiv.) in CH_3CN (5 mL). After addition of H_2O (1 mL) the mixture was filtered. Slow diffusion of methyl *tert*-butyl ether into the filtrate provided dark green crystals, which were suitable for single-crystal X-ray diffraction. The crystals were filtered off and washed three times with Et_2O. Yield: 68 mg (53 μmol, 53%). ESI-MS (pos. mode, CH_3CN): m/z = 883.1 $[(Htom^{6\text{-}Me})\{Ni^{II}(\mu\text{-glut})Ni^{II}\}]^+$, 442.1 $\{[(Htom^{6\text{-}Me})\{Ni^{II}(\mu\text{-glut})Ni^{II}\}]^+ + H^+\}^{2+}$. IR (KBr): $\tilde{\nu}/cm^{-1}$ = 3158 w, 3114 w, 3054 m, 3030 m, 2998 w, 2983 w, 2928 w, 2907 w, 2845 w, 2248 w, 2004 w, 1951 w, 1885 w, 1826 w, 1769 w, 1608 s, 1579 s, 1530 s, 1468 s, 1449 w, 1437 w, 1399 s, 1370 m, 1335 m, 1304 m, 1286 w, 1274 w, 1244 w, 1225 w, 1203 w, 1185 w, 1165 m, 1139 m, 1121 w, 1098 w, 1085 w, 1056 m, 1032 w, 1017 m, 1000 w, 968 m, 937 w, 922 w, 885 w, 860 w, 832 m, 791 m, 749 w, 734 s, 708 s, 669 w, 660 w, 644 w, 624 w, 611 m, 561 w, 512 m, 489 w, 453 w, 438 w. UV-Vis-NIR (2,2,2-trifluoroethanol): $\tilde{\nu}/cm^{-1}$ (ε/M^{-1} cm^{-1}) = 42 900 (46 000), 38 400 (17 700), 37 700 (17 600), 36 500 (13 200), 30 900 (4990), 29 300 (7880), 28 200 (10 270), 22 300 (30), 21 300 (27), 20 900 (28), 20 000 (19), 19 600 (21), 16 400 (21), 12 590 (11), 10 180 (30). Anal. calcd for $[(Htom^{6\text{-}Me})\{Ni^{II}(\mu\text{-glut})Ni^{II}\}](BPh_4)\cdot 2CH_3CN$ ($C_{73}H_{73}N_8O_6BNi_2$): C 68.15, H 5.72, N 8.71%. Found: C 67.84, H 5.76, N 8.57%.

Crystal structure determination

Single-crystals were removed from the mother liquor, coated with oil, and measured at 100(2) K on a Bruker KAPPA APEX II four-circle diffractometer equipped with 4K CCD detector. MoKα radiation with a focusing graphite monochromator was used to measure the crystals. Absorption was corrected numerically for $[(Htom^{6\text{-}Me})\{Ni^{II}(\mu\text{-glut})Ni^{II}\}](BPh_4)\cdot 2CH_3CN$ and using equivalent reflections for $[(Htom^{6\text{-}Me})\{Ni^{II}(\mu\text{-succ})Ni^{II}\}](BPh_4)\cdot 2CH_3CN$. Corrections were performed with the program SADABS-2016/2.[13] The structures were solved and refined *vs.* F^2 with the programs SHELXT/L[14] using OLEX2.[15]

The hydrogen atom between O1 and O3 was found and refined, all other hydrogen positions were generated for all structures. $[(Htom^{6\text{-}Me})\{Ni^{II}(\mu\text{-succ})Ni^{II}\}](BPh_4)\cdot 2CH_3CN$ shows pseudo-symmetry along a C_2 axis through C5 and C6, while $[(Htom^{6\text{-}Me})\{Ni^{II}(\mu\text{-glut})Ni^{II}\}](BPh_4)\cdot 2CH_3CN$ shows pseudo *C*-centration.

CCDC numbers 2445426–2445427† contain the supplementary crystallographic data for this paper.

Other physical measurements

Infrared spectra (400–4000 cm^{-1}) of solid samples were recorded on a Bruker Vertex 70 as KBr disks. ESI mass spectra were recorded on a Bruker Esquire 3000 ion trap mass spectrometer equipped with a standard ESI source. Elemental analyses were carried out on a HEKAtech Euro EA analyzer. UV-Vis-NIR absorption spectra were measured on a JASCO V770 spectrophotometer at 20 °C. Magnetic susceptibility data were measured on powdered samples in the temperature range 2–300 K by using a SQUID magnetometer (Quantum Design MPMS XL-7 EC) with a field of 1.0 T. Variable-temperature variable-field (VTVH) measurements were performed in various static fields (1–7 T) in the range 2–10 K with the magnetization equidistantly sampled on a $1/T$ temperature scale. For calculations of the molar magnetic susceptibilities, χ_m, the measured susceptibilities were corrected for the underlying diamagnetism of the sample holder and the sample by using tabulated Pascal's constants. The susceptibility data were analyzed using the program package JulX written by Eckhard Bill for spin-Hamiltonian simulations and fittings of the data by a full-matrix diagonalization approach. Magnetic moments were obtained from numerically generated derivatives of the eigenvalues of eqn (1), and summed up over 16 field orientations along a 16-point Lebedev grid to account for the powder distribution of the sample.

Results and discussion

Synthesis

We have recently shown that the coordinated acetates in the cytotoxic complex $[(Htom^{6\text{-}Me})\{Cu^{II}(OAc)\}_2](OAc)$ can be de-coordinated by protonation delivering HOAc resulting in the complex $[(Htom^{6\text{-}Me})\{Cu^{II}(OH_2)\}_2]^{3+}$.[16] Moreover, we have shown that the reaction of the dicopper complex $[(Htom^{6\text{-}Me})\{Cu^{II}(OH_2)\}_2]^{3+}$ in CH_3CN with a mixture of glutaric acid and NEt_3

provided the tetranuclear macrocycle $[\{(Htom^{6\text{-}Me})Cu^{II}_2\}_2(\mu\text{-glut})_2]^{2+}$.[12] In order to evaluate the influence of the metal ion on the coordination mode, we thought to use the also cytotoxic dinickel complex $[(Htom^{6\text{-}Me})\{Ni^{II}(OAc)\}_2](OAc)$ to obtain upon protonation the corresponding aqua complex $[(Htom^{6\text{-}Me})\{Ni^{II}(OH_2)_2\}_2]^{3+}$ for the reaction with dicarboxylic acids.

The reaction of $[(Htom^{6\text{-}Me})\{Ni^{II}(OAc)\}_2](OAc)$ with 3 equiv. of HCl in a mixture of MeOH/H_2O provides after addition of $NaBPh_4$ a precipitate. Based on our previous results, this procedure should deliberate the coordinated acetates and protonate the free acetates to acetic acid providing presumably $[(Htom^{6\text{-}Me})\{Ni^{II}(OH_2)_2\}_2](BPh_4)_3$. This precipitate was redissolved in CH_3CN with a small amount of H_2O. Reaction with 2.1 equiv. NEt_3 and either 1 equiv. succinic acid or glutaric acid provides the complexes $[(Htom^{6\text{-}Me})\{Ni^{II}(\mu\text{-succ})Ni^{II}\}](BPh_4)$ and $[(Htom^{6\text{-}Me})\{Ni^{II}(\mu\text{-glut})Ni^{II}\}](BPh_4)$, respectively (Scheme 2).

The FTIR spectra of $[(Htom^{6\text{-}Me})\{Ni^{II}(\mu\text{-succ})Ni^{II}\}](BPh_4)$ and $[(Htom^{6\text{-}Me})\{Ni^{II}(\mu\text{-glut})Ni^{II}\}](BPh_4)$ and for comparison of $[(Htom^{6\text{-}Me})\{Ni(OAc)\}_2](BPh_4)$[7] (Fig. 1 and S1†) are almost superimposable and show the characteristic bands of the coordinated pyridines at 1608 and 1579 cm^{-1}. Slight but significant differences were observed for the stretching modes $\nu_{as}(CO_2^-)$ and $\nu_s(CO_2^-)$ in the ranges 1530–1540 and 1450–1470 cm^{-1}, respectively (Fig. 1). The differences $\Delta(\nu_{as}\text{–}\nu_s)$ of 78 cm^{-1} for OAc^-, 62 cm^{-1} for $glut^{2-}$, and 91 cm^{-1} for $succ^{2-}$ indicate a bidentate binding mode of the carboxylates but with slight structural variations.[17] $[(Htom^{6\text{-}Me})\{Ni^{II}(\mu\text{-succ})Ni^{II}\}](BPh_4)$ shows one extra band at 892 cm^{-1} that might be characteristic for the succinate ligand.

Structural characterization

The complexes $[(Htom^{6\text{-}Me})\{Ni^{II}(\mu\text{-succ})Ni^{II}\}](BPh_4)\cdot 2CH_3CN$ and $[(Htom^{6\text{-}Me})\{Ni^{II}(\mu\text{-glut})Ni^{II}\}](BPh_4)\cdot 2CH_3CN$ crystallize with one complex in the asymmetric unit, *i.e.* without crystallographically imposed symmetry although the two complexes are close to C_2 symmetry (Fig. 2). The overall molecular structures are very similar with the N_3 binding pockets coordinating facially to the Ni^{II} ions. The octahedral coordination environments are completed by bidentate carboxylates and the naphthalenediolato donors.

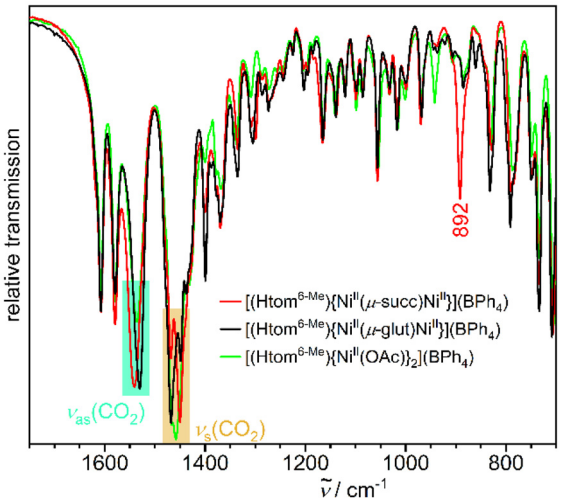

Fig. 1 FTIR spectra of $[(Htom^{6\text{-}Me})\{Ni^{II}(\mu\text{-succ})Ni^{II}\}](BPh_4)$, $[(Htom^{6\text{-}Me})\{Ni^{II}(\mu\text{-glut})Ni^{II}\}](BPh_4)$, and $[(Htom^{6\text{-}Me})\{Ni^{II}(OAc)\}_2](BPh_4)$[7] for comparison.

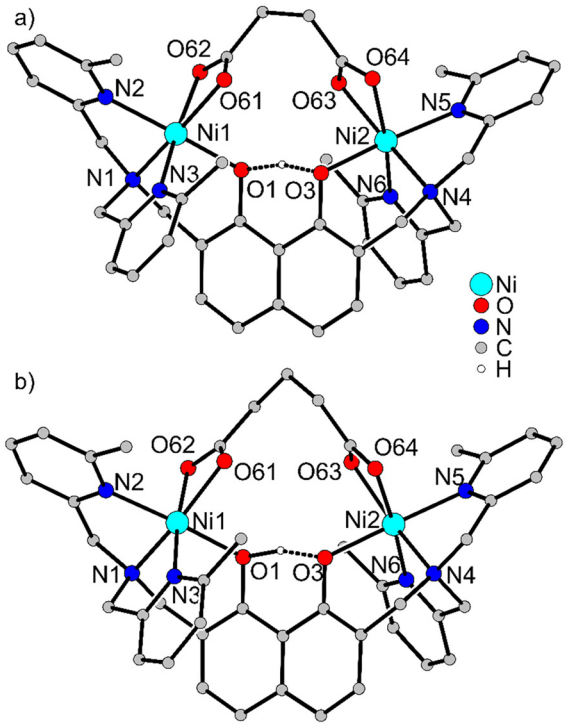

Fig. 2 Molecular structures of (a) $[(Htom^{6\text{-}Me})\{Ni^{II}(\mu\text{-succ})Ni^{II}\}]^+$ in single-crystals of $[(Htom^{6\text{-}Me})\{Ni^{II}(\mu\text{-succ})Ni^{II}\}](BPh_4)\cdot 2CH_3CN$ and (b) $[(Htom^{6\text{-}Me})\{Ni^{II}(\mu\text{-glut})Ni^{II}\}]^+$ in single-crystals of $[(Htom^{6\text{-}Me})\{Ni^{II}(\mu\text{-glut})Ni^{II}\}](BPh_4)\cdot 2CH_3CN$. Hydrogen atoms except those bound at oxygen atoms have been omitted for clarity.

The coordination around the Ni^{II} ions differs slightly for the two complexes. To evaluate the influence of the organic spacer, these variations are analyzed using the molecular structure of $[(Htom^{6\text{-}Me})\{Ni^{II}(OAc)\}_2](BPh_4)$[7] with monodentate acetates as reference. Fig. 3 shows on the left side truncated structures including selected bond lengths and on the right side an orientation viewing from the top of the acetates with the naphthalene unit almost perpendicular to the projection plane. Differences in bond lengths are emphasized only if they are outside the $\pm 3\sigma$ range (Table 1).

The coordination of the carboxylates is the same for all three complexes (central coordination site A as defined in ref. 9). The Ni1–Ni2 distance is 5.72 Å in $[(Htom^{6\text{-}Me})\{Ni^{II}(OAc)\}_2]^+$ (Fig. 3e), that decreases only slightly in $[(Htom^{6\text{-}Me})\{Ni^{II}(\mu\text{-glut})Ni^{II}\}]^+$ to 5.69 Å (Fig. 3c) but strongly to 5.12 Å in $[(Htom^{6\text{-}Me})\{Ni^{II}(\mu\text{-succ})Ni^{II}\}]^+$ (Fig. 3a) indicating that the shorter ethylene spacer of succinate exerts a strong pull effect on the two coordinated carboxylates. This pull effect is also nicely reflected by the distance between the carbon atoms of the methyl groups of the acetates of 3.78 Å in $[(Htom^{6\text{-}Me})\{Ni^{II}(OAc)\}_2]^+$ (Fig. 3f, carbon atoms highlighted in dark grey). This distance

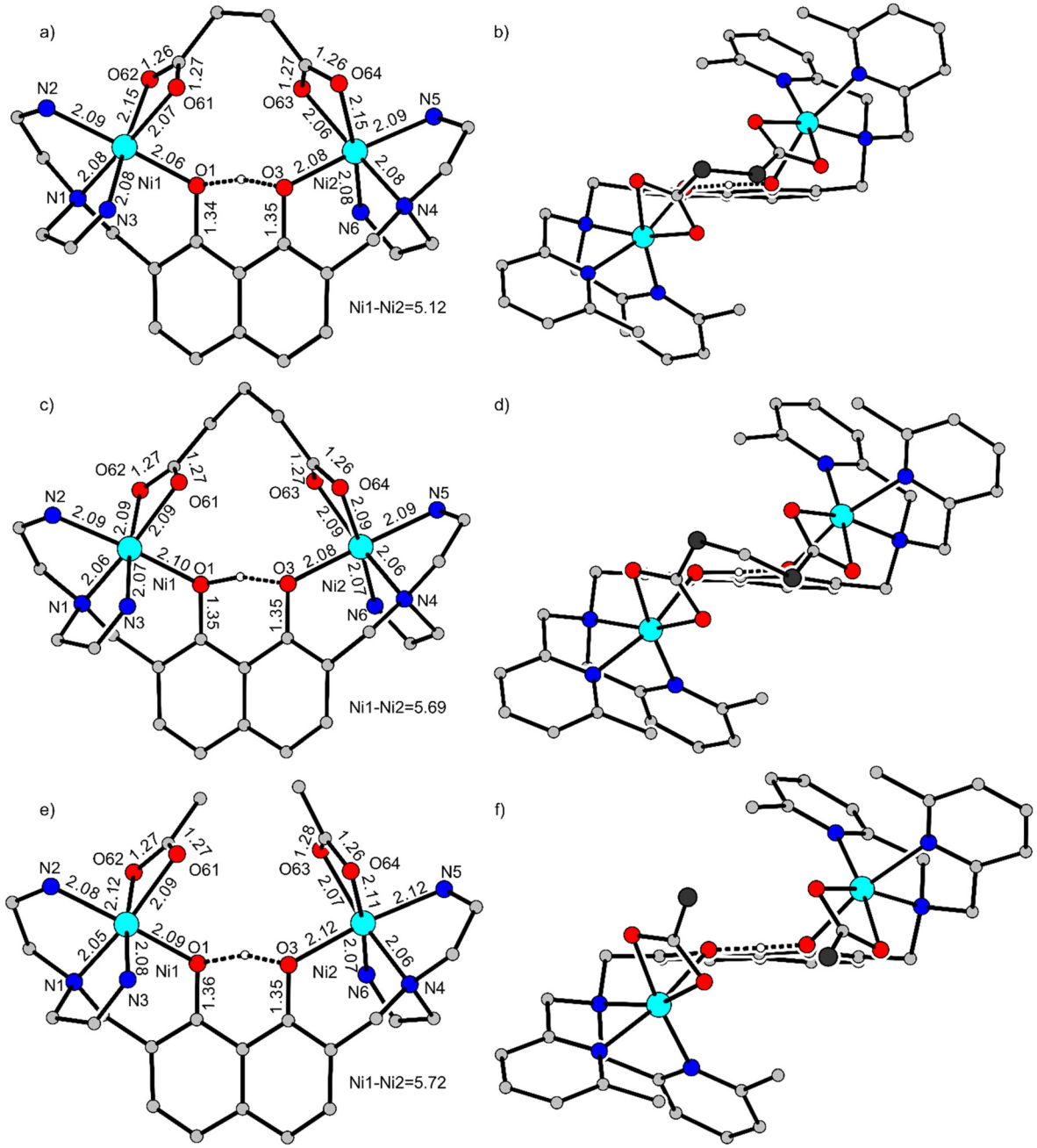

Fig. 3 Comparison of the molecular structures of (a) + (b) $[(Htom^{6\text{-}Me})\{Ni^{II}(\mu\text{-succ})Ni^{II}\}]^+$ in single-crystals of $[(Htom^{6\text{-}Me})\{Ni^{II}(\mu\text{-succ})Ni^{II}\}](BPh_4)\cdot 2CH_3CN$, (c) + (d) $[(Htom^{6\text{-}Me})\{Ni^{II}(\mu\text{-glut})Ni^{II}\}]^+$ in single-crystals of $[(Htom^{6\text{-}Me})\{Ni^{II}(\mu\text{-glut})Ni^{II}\}](BPh_4)\cdot 2CH_3CN$, and (e) + (f) $[(Htom^{6\text{-}Me})\{Ni^{II}(OAc)\}_2]^+$ in single-crystals of $[(Htom^{6\text{-}Me})\{Ni(OAc)\}_2](BPh_4)\cdot CH_2Cl_2$.[7] Left side: Molecular structures with selected bond lengths (Å) and with the pyridine donors truncated for clarity. Right side: View from the top of the carboxylate ligands with the naphthalene units oriented almost perpendicular to the projection plane. The methyl groups of the acetates in (f) and the corresponding carbon atoms in (b) and (d) are highlighted with larger spheres and dark grey filling.

decreases for the corresponding carbon atoms by insertion of a bridging methylene unit in $[(Htom^{6\text{-}Me})\{Ni^{II}(\mu\text{-glut})Ni^{II}\}]^+$ to 2.63 Å (Fig. 3d) and more extremely by connecting those two methyl groups to one ethylene bridge in $[(Htom^{6\text{-}Me})\{Ni^{II}(\mu\text{-succ})Ni^{II}\}]^+$ to 1.53 Å. This increased pull effect of the organic spacers also affects slightly the mean Ni–O^{naph} bond length that decreases from 2.11 Å in $[(Htom^{6\text{-}Me})\{Ni^{II}(OAc)\}_2]^+$ to 2.09 Å in $[(Htom^{6\text{-}Me})\{Ni^{II}(\mu\text{-glut})Ni^{II}\}]^+$ and to 2.07 Å in $[(Htom^{6\text{-}Me})\{Ni^{II}(\mu\text{-succ})Ni^{II}\}]^+$. The mean Ni–$O^{carb}$ bond lengths are slightly longer for the carboxylate oxygen atoms coordinated *trans* to a pyridine. This asymmetry in the mean Ni–O^{carb} distances (0.03 Å in $[(Htom^{6\text{-}Me})\{Ni^{II}(OAc)\}_2]^+$) almost vanishes in $[(Htom^{6\text{-}Me})\{Ni^{II}(\mu\text{-glut})Ni^{II}\}]^+$ but increases significantly to 0.08 Å in $[(Htom^{6\text{-}Me})\{Ni^{II}(\mu\text{-succ})Ni^{II}\}]^+$. It is interest-

Table 1 Selected interatomic distances (Å) and angles (°)

	[(Htom$^{6\text{-Me}}$){Ni^{II}(μ-succ)Ni^{II}}]$^+$		[(Htom$^{6\text{-Me}}$){Ni^{II}(μ-glut)Ni^{II}}]$^+$	
	Ni1	Ni2[a]	Ni1	Ni2[a]
Ni1–O1	2.0585(9)	2.0787(9)	2.1027(9)	2.0780(9)
Ni1–N1	2.0779(11)	2.0784(11)	2.0608(11)	2.0623(11)
Ni1–N2	2.0873(11)	2.0868(11)	2.0924(11)	2.0882(11)
Ni1–N3	2.0819(11)	2.0775(11)	2.0681(10)	2.0726(10)
Ni1–O61	2.0648(9)	2.0636(9)	2.0898(9)	2.0870(9)
Ni1–O62	2.1465(10)	2.1499(10)	2.0932(9)	2.0940(9)
Ni1···Ni2	5.5239(4)		5.6904(4)	
O1–Ni1–N1	89.90(4)	89.25(4)	90.72(4)	91.61(4)
O1–Ni1–N2	165.63(4)	164.85(4)	167.50(4)	167.81(4)
O1–Ni1–N3	92.33(4)	92.41(4)	89.86(4)	90.59(4)
O1–Ni1–O61	85.96(4)	86.02(4)	86.05(4)	87.55(4)
O1–Ni1–O62	85.77(4)	85.36(4)	85.74(4)	85.90(4)
N1–Ni1–N2	79.91(4)	79.56(4)	79.97(4)	80.02(4)
N1–Ni1–N3	82.49(4)	83.50(4)	83.84(4)	82.67(4)
N1–Ni1–O61	166.50(4)	166.63(4)	162.68(4)	162.87(4)
N1–Ni1–O62	104.16(4)	104.44(4)	99.68(4)	99.67(4)
N2–Ni1–N3	96.31(4)	96.39(4)	97.34(4)	97.06(4)
N2–Ni1–O61	101.63(4)	102.59(4)	100.36(4)	97.82(4)
N2–Ni1–O62	86.93(4)	87.56(4)	87.62(4)	86.78(4)
N3–Ni1–O61	110.49(4)	109.16(4)	113.12(4)	114.45(4)
N3–Ni1–O62	173.06(4)	171.70(4)	174.39(4)	175.82(4)
O61–Ni1–O62	62.75(4)	62.75(4)	63.14(4)	63.20(4)

[a] The numbering scheme of the Ni2 side or molecule has been adapted according to the Ni1 side.

ing to note, that these asymmetries correlate with the difference of the vibrational modes $\Delta(\nu_{as}-\nu_s)$ of the carboxylates, which is the largest for succinate and the smallest for glutarate. Thus, the carboxylate stretching modes reflect the pull effect of the organic spacers.

Magnetic properties

The magnetic data of both complexes are shown in Fig. 4. The effective magnetic moment, μ_{eff}, is almost temperature independent but decreases slightly below 30 K. This behavior can be attributed to a weak antiferromagnetic interaction or to zero-field-splitting or to a combination of both but cannot be differentiated from the simulation of μ_{eff} *vs.* T alone. However, the variable field–variable temperature (VTVH) magnetization data show a nesting behavior of the isofield lines indicating the presence of significant zero-field splitting.[18] The simultaneous simulation of the μ_{eff} *vs.* T and the VTVH data allows to analyze these contributions. Therefore, we have simulated and fitted the magnetic data using the spin-Hamiltonian (eqn (1)).

$$\hat{\boldsymbol{H}} = -2J\hat{\boldsymbol{S}}_1\hat{\boldsymbol{S}}_2 + \sum_{i=1}^{2} D_i\hat{S}_{z,i}^2 + \sum_{i=1}^{2} g\mu_B\hat{\boldsymbol{S}}_i\boldsymbol{B} \quad (1)$$

The first term is the isotropic HDvV exchange Hamiltonian, the second term the local axial zero-field splitting, and the last term the local Zeeman Hamiltonian. The simultaneous simulation and fitting provided the parameter sets given in Fig. 4. Please note that the signs of D_i correspond only to the fits provided but are not determined by these powder measurements.

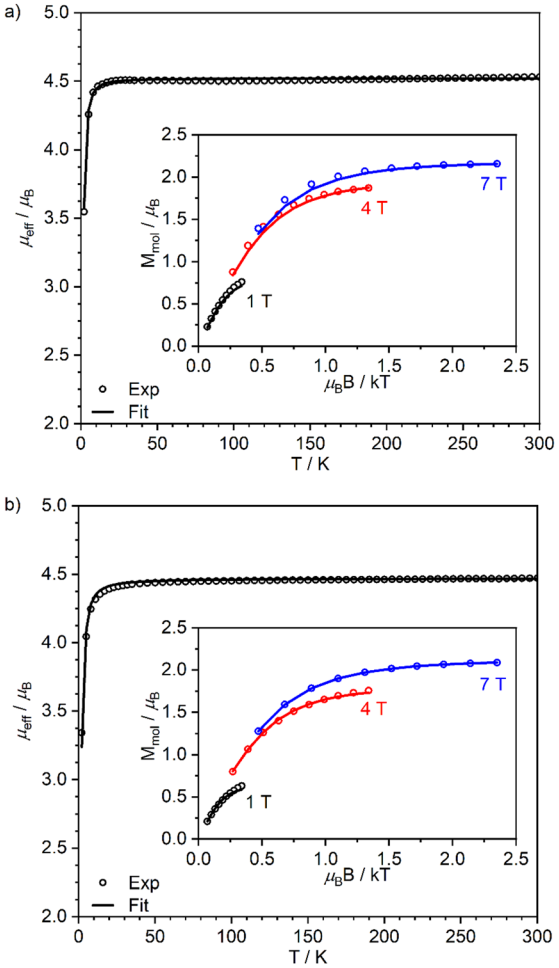

Fig. 4 Temperature-dependence of the effective magnetic moment, μ_{eff}, of (a) [(Htom$^{6\text{-Me}}$){Ni^{II}(μ-succ)Ni^{II}}](BPh$_4$)·2CH$_3$CN and (b) [(Htom$^{6\text{-Me}}$){Ni^{II}(μ-glut)Ni^{II}}](BPh$_4$)·2CH$_3$CN: and variable-field variable-temperature (VTVH) magnetization data in the insets. The solid lines correspond to spin-Hamiltonian fits with the following parameter sets: (a) J_{12} = −0.075 cm^{-1}, g_i = 2.26, D_i = 3.50 cm^{-1}, χ_{TIP} = 50 × 10^{-6} cm^3 mol^{-1}, (b) J_{12} = −0.20 cm^{-1}, g_i = 2.235, D_i = 4.00 cm^{-1}, χ_{Tip} = 150 × 10^{-6} cm^3 mol^{-1}. Contributions from χ_{TIP} were subtracted from experimental and simulated data.

Both complexes exhibit very small antiferromagnetic exchange and a moderate zero-field splitting parameter. There is no correlation between the exchange coupling constant J and the slight variation of the Ni–O^{naph} bond lengths, which should mainly influence the exchange pathway.

UV-Vis-NIR spectroscopy

The UV-Vis-NIR spectra of [(Htom$^{6\text{-Me}}$){Ni^{II}(μ-succ)Ni^{II}}](BPh$_4$) and [(Htom$^{6\text{-Me}}$){Ni^{II}(μ-glut)Ni^{II}}](BPh$_4$) are shown with [(Htom$^{6\text{-Me}}$){Ni^{II}(OAc)}$_2$](OAc) as reference in Fig. 5. The spectra exhibit above 25 000 cm^{-1} the typical π → π* transitions and below 25 000 cm^{-1} the typical d–d transitions of Ni^{II}. Although the differences are not tremendous, the $^3A_{2g}(F)$ → $^3T_{2g}(F)$ and $^3A_{2g}(F)$ → $^3T_{1g}(F)$[19] are slightly shifted to higher energies for [(Htom$^{6\text{-Me}}$){Ni^{II}(μ-succ)Ni^{II}}]$^+$ (10 280 and

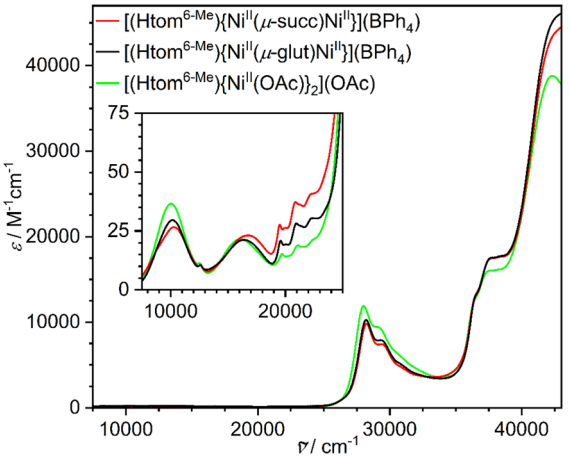

Fig. 5 Electronic absorption spectra of $[(Htom^{6\text{-}Me})\{Ni^{II}(\mu\text{-succ})Ni^{II}\}](BPh_4)$ and $[(Htom^{6\text{-}Me})\{Ni^{II}(\mu\text{-glut})Ni^{II}\}](BPh_4)$ in 2,2,2-trifluoroethanol and of $[(Htom^{6\text{-}Me})\{Ni^{II}(OAc)\}_2](OAc)$[7] in CH_3CN for comparison. 2,2,2-Trifluorethanol was used as solvent as (*i*) those two complexes were not soluble enough in CH_3CN for concentrated solutions required for measuring the d–d transitions and (*ii*) we have had a good experience previously[16] with 2,2,2-trifluoroethanol as a slightly polar solvent without strong coordinating properties.

16 770 cm^{-1}) than in $[(Htom^{6\text{-}Me})\{Ni^{II}(\mu\text{-glut})Ni^{II}\}]^+$ (10 180 and 16 400 cm^{-1}), and $[(Htom^{6\text{-}Me})\{Ni^{II}(OAc)\}_2]^+$ (10 060 and 16 100 cm^{-1}). This higher ligand field in $[(Htom^{6\text{-}Me})\{Ni^{II}(\mu\text{-succ})Ni^{II}\}]^+$ correlates with the shorter Ni–O^{naph} bond lengths and the stronger Ni–O^{carb} asymmetry (one shorter Ni–O^{carb} bond) induced by the shorter ethylene spacer between the two coordinated carboxylates. Extraction of the Racah parameter *B* from these transitions[20] provides 850 cm^{-1} for both $[(Htom^{6\text{-}Me})\{Ni^{II}(\mu\text{-glut})Ni^{II}\}]^+$ and $[(Htom^{6\text{-}Me})\{Ni^{II}(OAc)\}_2]^+$ but 940 cm^{-1} for $[(Htom^{6\text{-}Me})\{Ni^{II}(\mu\text{-succ})Ni^{II}\}]^+$. The significantly higher value for $[(Htom^{6\text{-}Me})\{Ni^{II}(\mu\text{-succ})Ni^{II}\}]^+$ indicates an overall lower covalence of the Ni^{II}–ligand bonds, *i.e.* the higher covalence of the shorter Ni–O^{naph} is overcompensated by the other bonds leading an overall lower covalence of the Ni^{II} ion.

Conclusion

It is assumed that the cytotoxicity of the dinuclear complex $[(Htom^{6\text{-}Me})\{Ni^{II}(OAc)\}_2](OAc)$ is based on the substitution of the acetates by H_2O ligands in aqueous media forming the complex $[(Htom^{6\text{-}Me})\{Ni^{II}(OH_2)_2\}_2]^{3+}$ and that after electrostatic attraction by the polyanionic DNA the complex fragment $[(Htom^{6\text{-}Me})Ni^{II}_2]^{3+}$ binds to two neighboring phosphate diesters of the DNA backbone. This molecular mode of action has been mimicked by protonation of the acetates forming presumably $[(Htom^{6\text{-}Me})\{Ni^{II}(OH_2)_2\}_2]^{3+}$ that reacts with the difunctional donors succinate and glutarate providing the anticipated complexes $[(Htom^{6\text{-}Me})\{Ni^{II}(\mu\text{-succ})Ni^{II}\}]^+$ and $[(Htom^{6\text{-}Me})\{Ni^{II}(\mu\text{-glut})Ni^{II}\}]^+$, respectively. The comparison of the molecular structures of these two complexes with that of $[(Htom^{6\text{-}Me})\{Ni^{II}(OAc)\}_2]^+$ as reference demonstrates a pull effect of the organic spacer that is stronger the shorter the spacer is. FTIR and UV-Vis-NIR spectroscopies reflect the induced changes on Ni^{II} coordination environment indicating the potential to serve as spectroscopic probes. The coordination compartments show enough flexibility to compensate for this pull effect demonstrating the flexibility despite the rigid 1,8-naphthalenediol backbone.

It seems to be worthwile to speculate on the origin of the different complexes obtained from $[(Htom^{6\text{-}Me})M^{II}_2]^{3+}$ with glutarate for Ni^{II} (dinuclear complex with intramolecularly bridging glutarate) and Cu^{II} (tetranuclear complex with intermolecularly bridging glutarates).[12] Ni^{II} ions with this donor set prefer six-coordination enforcing the carboxylates to bind in a bidentate fashion, while the Jahn–Teller active Cu^{II} ions prefer five-coordination with monodentate carboxylates. The 6-methyl groups of the pyridine donors exhibit sterical strain on ligands coordinated *cis* to the pyridine with the 6-methyl group pointing to these ligands.[21] As a consequence, the N_3 binding pockets prefer a facial binding to the Ni^{II} ions with bidentate carboxylates but a meridional binding to the Cu^{II} ions with monodentate carboxylates (Fig. 6).[7] This results in an orientation of the acetates in the Ni^{II} complexes turned towards each other (distance between the two carboxylate carbon atoms of 4.16 Å), while those in the Cu^{II} complexes are

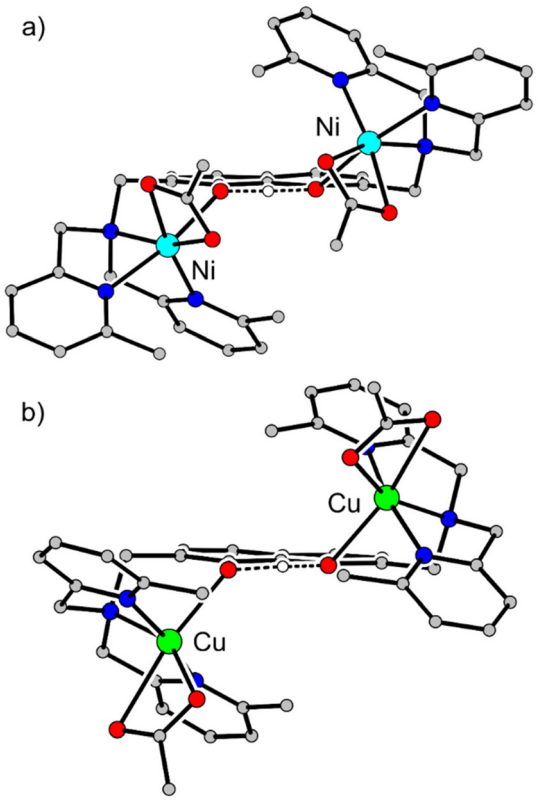

Fig. 6 Molecular structures of (a) $[(Htom^{6\text{-}Me})\{Ni^{II}(OAc)\}_2]^+$ and (b) $[(Htom^{6\text{-}Me})\{Cu^{II}(OAc)\}_2]^+$ to demonstrate the influence of the 6-methyl groups of the pyridines on the coordination mode of the N_3 ligand compartments and hence on the relative orientation of the acetates to each other.

turned away from each other (distance between the two carboxylate carbon atoms of 9.46 Å). The latter seems not only to be unfavorable for the intramolecular bridging mode of a dicarboxylate model but also for the intended coordination to two neighboring phosphate diesters of the DNA backbone. Thus, this study shows a severe impact of the 6-methyl groups of the pyridines on the coordination mode of the metal ions that could enforce sterical constraints for the binding to two neighboring phosphates of the DNA backbone and hence weaken the binding affinity. To prevent these sterical constraint from the beginning, the dinuclear Cu_2^{II} and Ni_2^{II} complexes without 6-methyl groups (*i.e.* $[(Htom)M_2^{II}]^{3+}$) could enhance the binding affinity to the DNA backbone enhancing the cytotoxicity. Corresponding studies have been started in our lab.

Data availability

The supplementary crystallographic data for this study have been deposited at the Cambridge Crystallographic Data Centre under accession codes 2445426–2445427.†

Conflicts of interest

The authors declare no competing financial interests.

Acknowledgements

Financial support from Bielefeld University is gratefully acknowledged.

References

1 B. Rosenberg and L. van Camp, *Nature*, 1965, **205**, 698–699.
2 (*a*) S. Dilruba and G. V. Kalayda, *Cancer Chemother. Pharmacol.*, 2016, **77**, 1103–1124; (*b*) S. Ghosh, *Bioorg. Chem.*, 2019, **88**, 102925; (*c*) S. Rottenberg, C. Disler and P. Perego, *Nat. Rev. Cancer*, 2021, **21**, 37–50; (*d*) C. Zhang, C. Xu, X. Gao and Q. Yao, *Theranostics*, 2022, **12**, 2115–2132; (*e*) T. C. Johnstone, K. Suntharalingam and S. J. Lippard, *Chem. Rev.*, 2016, **116**, 3436–3486; (*f*) Y. Jung and S. J. Lippard, *Chem. Rev.*, 2007, **107**, 1387–1407.
3 (*a*) R. Oun, Y. E. Moussa and N. J. Wheate, *Dalton Trans.*, 2018, **47**, 6645–6653; (*b*) L. Kelland, *Nat. Rev. Cancer*, 2007, **7**, 573–584.
4 (*a*) S. Sen, M. Won, M. S. Levine, Y. Noh, A. C. Sedgwick, J. S. Kim, J. L. Sessler and J. F. Arambula, *Chem. Soc. Rev.*, 2022, **51**, 1212–1233; (*b*) D. Denoyer, S. Masaldan, S. La Fontaine and M. A. Cater, *Metallomics*, 2015, **7**, 1459–1476; (*c*) C. Santini, M. Pellei, V. Gandin, M. Porchia, F. Tisato and C. Marzano, *Chem. Rev.*, 2014, **114**, 815–862.
5 M. Mammen, S. K. Choi and G. M. Whitesides, *Angew. Chem., Int. Ed.*, 1998, **37**, 2755–2794.
6 T. Jany, A. Moreth, C. Gruschka, A. Sischka, A. Spiering, M. Dieding, Y. Wang, S. H. Samo, A. Stammler, H. Bögge, G. Fischer von Mollard, D. Anselmetti and T. Glaser, *Inorg. Chem.*, 2015, **54**, 2679–2690.
7 S. Schwarzbich, C. Horstmann née Gruschka, J. Simon, L. Siebe, A. Moreth, C. Wiegand, A. Lavrentieva, T. Scheper, A. Stammler, H. Bögge, G. Fischer von Mollard and T. Glaser, *Inorg. Chem.*, 2020, **59**, 14464–14477.
8 J. Simon, A. Stammler, J. Oldengott, H. Bögge and T. Glaser, *Inorg. Chem.*, 2020, **59**, 14615–14619.
9 J. Simon, C. Horstmann née Gruschka, A. Mix, A. Stammler, J. Oldengott, H. Bögge and T. Glaser, *Dalton Trans.*, 2022, **51**, 2863–2875.
10 M. Giampà, D. Corinti, A. Maccelli, S. Fornarini, G. Berden, J. Oomens, S. Schwarzbich, T. Glaser and M. E. Crestoni, *Inorg. Chem.*, 2023, **62**, 1341–1353.
11 N. Biere, D. Kreft, V. Walhorn, S. Schwarzbich, T. Glaser and D. Anselmetti, *J. Nanobiotechnol.*, 2023, **21**, 26.
12 T. Riediger, Z. Aydin, A. Stammler, J. Oldengott and T. Glaser, *Z. Anorg. Allg. Chem.*, 2024, e202300231.
13 *SADABS*, Bruker AXS Inc., Madison, Wisconsin, USA, 2012.
14 (*a*) G. M. Sheldrick, *Acta Crystallogr., Sect. A: Found. Crystallogr.*, 2008, **64**, 112–122; (*b*) G. M. Sheldrick, *Acta Crystallogr., Sect. A: Found. Adv.*, 2015, **71**, 3–8; (*c*) G. M. Sheldrick, *Acta Crystallogr., Sect. C: Struct. Chem.*, 2015, **71**, 3–8.
15 O. V. Dolomanov, L. J. Bourhis, R. J. Gildea, J. A. K. Howard and H. Puschmann, *J. Appl. Crystallogr.*, 2009, **42**, 339–341.
16 T. Riediger, A. Stammler, J. Oldengott, S. Walleck and T. Glaser, *Inorg. Chem.*, 2025, **64**, 9035–9043.
17 G. Deacon and R. J. Phillips, *Coord. Chem. Rev.*, 1980, **33**, 227–250.
18 J.-J. Girerd and Y. Journaux, in *Physical Methods in Bioinorganic Chemistry*, ed. L. Que Jr., University Science Books, Sausalito, 2000, pp. 321–374.
19 (*a*) T. R. Holman, M. P. Hendrich and L. Que Jr., *Inorg. Chem.*, 1992, **31**, 937–939; (*b*) L. C. Nathan, J. H. Nelson, G. L. Rich and R. O. Ragsdale, *Inorg. Chem.*, 1969, **8**, 1494–1497; (*c*) R. Whyman, W. E. Hatfield and J. S. Paschal, *Inorg. Chim. Acta*, 1967, **1**, 113.
20 A. B. P. Lever, *J. Chem. Educ.*, 1968, **45**, 711–712.
21 T. P. Zimmermann, S. Dammers, A. Stammler, H. Bögge and T. Glaser, *Eur. J. Inorg. Chem.*, 2018, **48**, 5229–5237.